Available online at www.sciencedirect.com
ScienceDirect
Ceramics International 37 (2011) 797–802
CERAMICS INTERNATIONAL
www.elsevier.com/locate/ceramint

Mesoporous high surface area $Ce_{0.9}Gd_{0.1}O_{1.95}$ synthesized by spray drying

Mats Lundberg [1,2], Hsiang-Jen Wang [1], Peter Blennow [1,*], Mohan Menon [1,3]

Fuel Cells and Solid State Chemistry Division, Risø National Laboratory for Sustainable Energy, Technical University of Denmark, DK-4000 Roskilde, Denmark

Received 28 June 2010; received in revised form 14 September 2010; accepted 8 October 2010
Available online 17 November 2010

Abstract

Mesoporous gadolinium doped cerium dioxide with high surface area was produced by spray drying using Pluronic 123 as surfactant. The powder, when calcined at 400 °C, had a BET surface area of 136 $m^2\ g^{-1}$ and was polycrystalline as confirmed by XRD and TEM. XEDS confirmed Ce, Gd and O, as the only elements present in the powders. Nitrogen adsorption measurements showed that the material was mesoporous with pore diameters of approximately 10 nm, which was later confirmed by TEM studies. TEM–EELS were used to confirm that Ce was in the +4 oxidation state. SEM studies showed particles of 10 nm diameter, corresponding to the crystallite size calculated from XRD data. The similar size range of the mesopores and the observed crystallite size indicates that the porosity is partly formed from intergranular mesoporosity. Using the spray drying method of a surfactant assisted liquid precursor solution it can be possible to manufacture mesoporous gadolinium doped ceria in large quantities in a continuous production.

Keywords: Electron microscopy; Cerium dioxide; Spray drying; Mesoporous

1. Introduction

Cerium dioxide is widely used as a promoter in the so-called "three-way catalyst" for the elimination of toxic exhaust gases in automobiles. The key property of ceria is to store and release oxygen [1]. Incorporation of various dopants such as La^{3+} [2], Y^{3+} [3], Ca^{2+}/Pb^{2+}/Nd^{3+} [4], and Zr^{4+} [5], in the cerium dioxide lattice have been shown to improve the thermal stability, altered catalytic properties, and possibly give different adsorptive properties. Gd^{3+} has been used as dopant in cerium dioxide for use in solid oxide fuel cells (SOFCs) for example; $Ce_{0.9}Gd_{0.1}O_{1.95}$ (CGO) is used both in electrolytes and electrodes [6]. Due to its high ionic conductivity at temperatures below 700 °C, CGO is an attractive candidate for electrolytes in intermediate-temperature solid oxide fuel cells (IT-SOFCs), especially at temperatures below 600 °C [7]. CGO exhibits promising catalytic activity for methane conversion and is therefore an alternative anode constituent in SOFC for direct methane conversion to avoid carbon deposition in Ni/YSZ anodes [8]. Furthermore, the high oxygen ion conductivity and oxygen reduction activity of CGO makes it an attractive candidate for use in composite cathodes in SOFC. The catalytic activity of CGO powders used in the SOFC electrodes depends on the surface area of the powders and is higher for powders with higher specific surface area. In order to produce high surface area CGO powders at relatively low cost, a continuous processing technique with high yield is required.

Mesoporous cerium dioxide with high surface area and high crystallinity has been reported previously by Lundberg et al. [1,9]. Their synthesis was based on a flash evaporation method of thin liquid films by a quick synthesis method. The porosity and high surface area in combination with high crystallinity is of interest for catalytic applications. The surface area was dependent on the thickness of the film when calcined. Lundberg et al. used the block co-polymer Pluronic 123 as the structure directing agent to create the mesoporous materials. It is possible to apply this synthesis route on gadolinium doped ceria, but the need of larger amounts of powder proves this synthesis route

* Corresponding author. Tel.: +45 4677 5868; fax: +45 4677 5858.
E-mail address: pebl@risoe.dtu.dk (P. Blennow).
[1] These authors have made an equal contribution to this article.
[2] Present address: Sandvik Materials Technology, Sandvik AB, 81181 Sandviken, Sweden.
[3] Present address: REC Wafer Norway AS, Tormod Gjestlandsvei 41, 3908 Porsgrunn, Norway.

0272-8842/$36.00
doi:10.1016/j.ceramint.2010.10.024

insufficient for large scale production. To our knowledge no reports on mesoporous CGO have been reported. Song et al. [10] have reported mesoporous yttrium doped CeO_2 using a chemical precipitation method.

Ceramic spray drying is a versatile and cheap powder processing method, which involve spraying a liquid suspension of the materials to agglomerate into a stream of heated air [11]. Spray drying is a proven method with high productivity and is used in variety of industries. The hypothesis we present in this work is that the droplets formed during the spray drying process can be controlled by the operating parameters and can be adjusted such that they are comparable to a thin film and could thus result in high surface area mesoporous CGO powders. Recently, CGO was synthesized by spray drying a water based solution of nitrate salts [12] to produce powders with a BET surface area of 70 $m^2\ g^{-1}$ (calcined at 300 °C). However, nitrogen adsorption measurements showed that these powders were not mesoporous.

In this work, 10 atom% gadolinium-doped ceria ($Ce_{0.9}Gd_{0.1}O_{1.95}$, CGO10) powders were synthesized by a surfactant assisted spray drying route and successive calcinations. The block co-polymer Pluronic 123 was used as the structure directing agent for the synthesis of the high-surface-area crystalline mesoporous CGO powder. The phase composition, morphology, size distribution and specific surface area of powders were characterized and compared to results obtained with CGO powders produced in the same manner without addition of P123 [12]. From this comparison, effect of P123 addition was evaluated.

2. Experimental

A 60 wt% CGO10 aqueous nitrate solution containing Ce^{3+}, Gd^{3+} cations in the mole ratio of 9:1 was prepared by dissolving calibrated $Ce(NO_3)_3{\cdot}6H_2O$ (99.9%, Alfa Aesar, Germany) and $Gd(NO_3)_3{\cdot}6H_2O$ (99.9%, Alfa Aesar, Germany) precursors. This corresponded to 133.4 g $Ce(NO_3)_3{\cdot}6H_2O$ and 15.4 g $Gd(NO_3)_3{\cdot}6H_2O$ in 40 g of water. To this solution 10 wt% (relative to water) block co-polymer Pluronic 123 (BASF SE, Germany) was added. After complete dissolution of all precursors and surfactant, the as-prepared solution was spray dried in a laboratory spray drier (B-290, BÜCHI, Switzerland) using the following process parameters: inlet temperature 220 °C, outlet temperature 145 °C, nozzle diameter 0.5 mm, spray flow 60 ml h^{-1}, air flow 660 l h^{-1}. The fabricated powders were subsequently calcined in a covered alumina crucible in the range of 300–600 °C with a dwell time of 2 h.

The phase composition after heat treatment was determined by powder X-ray diffraction (XRD) using a STOE Theta-Theta diffractometer. X-ray diffractograms were collected at $20^\circ \leq 2\theta \leq 90^\circ$ using Cu K_α radiation. The average grain size d_{avg} was calculated from the XRD diffractograms using Scherrer's equation:

$$d_a \approx \frac{\kappa \cdot \lambda}{\beta \cdot \cos(\theta)} \quad (1)$$

where κ, λ, β, and θ are the shape factor (taken as 0.9), the wave length of the Cu K_α radiation (1.54056 Å), the full width at half maximum (FWHM) of the reflections (corrected for instrument broadening), and the Bragg angle of the specific reflection, respectively.

The samples were examined by transmission electron microscopy (TEM) at 300 kV accelerating voltage (JEOL JEM-3000F, FEGTEM). For the primary TEM investigation the powder samples were suspended in ethanol and transferred to a copper–carbon grid by dipping into the suspension. Scanning TEM (STEM) investigations using high angle annular dark field detector (HAADF) were performed using the same instrument. X-ray energy-dispersive spectrometry (XEDS) spectra were collected in STEM mode at 300 kV using an Oxford EDS detector. Electron energy loss spectrometry (EELS) spectra were collected by a Gatan EELS detector at 297 kV.

The sample calcined at 400 °C was embedded in epoxy resin and subsequently polymerized at 70 °C for 16 h [13]. The embedded sample was sectioned by a Leica Ultra Cut UCT microtome, equipped with a diamond knife. The microtome sections were approximately 50 nm thick, judged by the light reflection of each cut when floating in fluid. The sections were collected on holey carbon grids before TEM observation.

Scanning electron microscopy (SEM) was used for surface studies at accelerating voltage of 5 kV (Zeiss Supra 35). X-ray energy-dispersive spectrometry (XEDS) was performed at 20 kV with a polymer window detector (Thermo Noran, detectable element $z \geq 5129$ eV Mn Kα).

BET specific surface area and pore size distribution were calculated from data collected on a Quantachrome Autosorb 1MP instrument, where all samples were degassed at 300 °C for at least 3 h prior to adsorption/desorportion. The BET surface areas were calculated from the adsorption isotherm keeping the values of p/p_0 between 0.05 and 0.30. The pore size distribution was calculated from the isotherms of the adsorption and desorption branches, respectively.

Weight loss and phase changes of the as-spray dried precursor solution as a function of temperature was characterized by a thermal analyzer (STA 449 Jupiter, Netzsch, Selb, Germany) capable of simultaneous thermogravimetry (TG) and differential thermal analysis (DTA). The thermal analysis was conducted in flowing air (50 ml min^{-1}) at a heating rate of 5 K min^{-1}.

3. Results and discussion

3.1. Powder synthesis and microstructural characterization

After spray drying of the aqueous precursor solution a white fine grained powder was obtained. Due to the low outlet temperature (145 °C) of the spray dryer it was clear that the as-synthesized powder could be treated as a precursor powder comprising a homogeneous mixture of nitrates, metal cations, and hydrocarbon species from the Pluronic P123. Similar observations were also shown previously [12]. Therefore, a calcinations step was needed to remove residual water and hydrocarbons and decompose the nitrate precursors to form the desired CGO10 powder. The powders expanded during the calcination step, most likely due to the gas evolution from the remaining water being evaporated in combination with the

evolution of gases caused by the decomposition of the hydrocarbons and the nitrates. The end volume was roughly ten times as large as the as-spray dried powder. This was not seen previously [12], when no P123 was used. Thus, the generally observed surfactant effect of the block co-polymer, i.e. forming of liquid crystalline shapes for the templating, in this case begins with the release of trapped gases (water evaporation and nitrate decomposition), causing a dramatic volume expansion. Following this volume expansion the decomposition temperature for the P123 is reached and the crystallization process of the CGO starts. This generates a very porous (both macroporous and mesoporous) solid network of the oxide phase.

To obtain micro-structural and morphological information of the calcined powders, all samples were first inspected with light microscope, followed by a detailed analysis utilizing SEM and TEM. The calcined powders were observed to be relatively fine and could be broken into even smaller pieces upon gentle grinding. A typical SEM overview image acquired from the powders calcined at 400 °C is given in Fig. 1(a), coupled with the corresponding high-resolution SEM image in Fig. 1(b). The images show that the porous particles comprised of agglomerates, where the walls contains numerous nanoparticles. By examining the image in Fig. 1(b), these nanoparticles were measured to be around 10 nm in diameter.

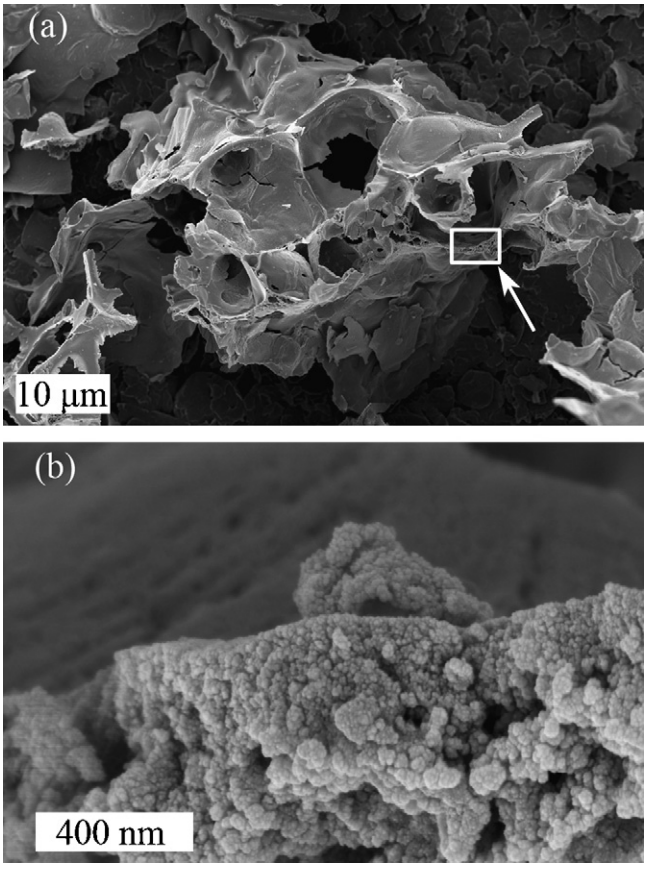

Fig. 1. SEM micrographs showing (a) the microstructure of the fine CGO10 powder calcined at 400 °C and (b) and the nanosized particles forming the walls of the microstructure. The square and arrow in (a) indicate the area where the higher resolution image in (b) was acquired.

3.2. XRD and BET

In Table 1 the calcination temperatures are given together with the resulting BET specific surface areas and the particle size of crystallites calculated from XRD using Eq. (1). XRD diffractogram of the powder calcined at 400 °C is shown in Fig. 2 together with the XRD pattern from a CGO10 powder sintered at 1500 °C in air for 4 h [12]. The diffractogram of the powder calcined at 400 °C was similar to the single phase diffractograms presented in Ref. [12] with broad peaks indicating a powder containing nano sized crystallites. The spray dried powder showed a maximum specific surface area of 136 $m^2\ g^{-1}$ at 400 °C. The specific surface area decreased as the calcination temperature increased. After calcination at 600 °C for 2 h the specific surface area was around 92 $m^2\ g^{-1}$, suggesting sufficient thermal stability. After calcination at 300 °C the crystallite size had the smallest value of approximately 8 nm. However, the calculated BET specific surface area was only 104 $m^2\ g^{-1}$, seemingly lower than the sample calcined at 500 °C. This is most likely explained by that there was still hydrocarbon residues present in the sample (from the Pluronic P123 surfactant) calcined at 300 °C, which would block some pores in the powder agglomerates giving a lower specific surface area. This hypothesis is strengthened by the thermal analysis discussed in Section 3.4.

The isotherms of all the prepared powders had type IV sorption isotherms [14] with hysteresis loop of H2 character [15], see Fig. 3. The size and structure of the pores will affect the shape of the isotherm. The H2 character of the hysteresis loop is typically an indication of disordered pores with poorly defined size and shape distribution. Furthermore, the characteristic hysteresis loop seen in Fig. 3 is normally associated with the occurrence of pore condensation typical for mesoporous materials. In Fig. 4 the adsorption–desorption pore volume plot is displayed for the sample calcined at 400 °C. The pore size distribution of mesoporous materials is usually calculated with the Barrett, Joyner and Halenda (BJH) method [16] by combining the Kelvin equation and the Halsey empirical equation. This method has been shown to underestimate the size of pores [17,18] and other calculation methods have been suggested to improve the accuracy [19–21] in the pore size determination below 120 Å. A major problem with nitrogen adsorption is that mesopores with pore diameters of 20–120 Å will be influenced by phenomena as e.g. the tensile strength effect (TSE) and fluid-to-crystalline like phase transitions of the adsorbed phase [22]. These phenomena will influence the desorption isotherm giving incorrect pore size

Table 1
Temperature study of the spray dried CGO10 powder. The crystallite sizes were calculated using Eq. (1).

Temperature (°C)	BET surface area ($m^2\ g^{-1}$)	Particle size of crystallites (nm)
300	104	8
400	136	9
500	110	10
600	92	14

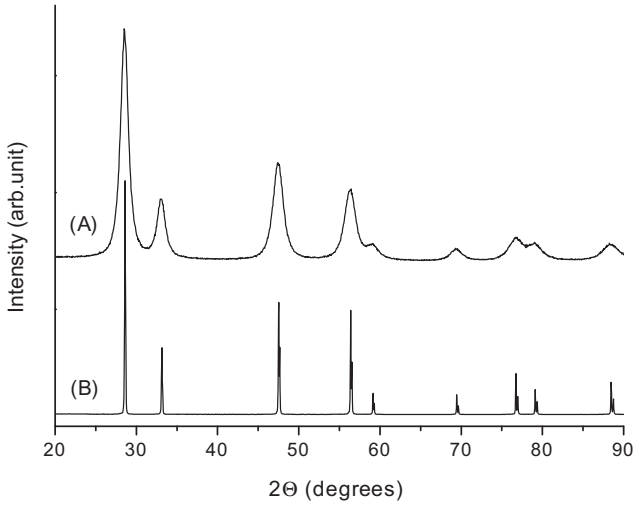

Fig. 2. XRD diffractograms of spray dried powder calcined at 400 °C (A) and after sintering a CGO10 powder [12] at 1500 °C for 4 h (B).

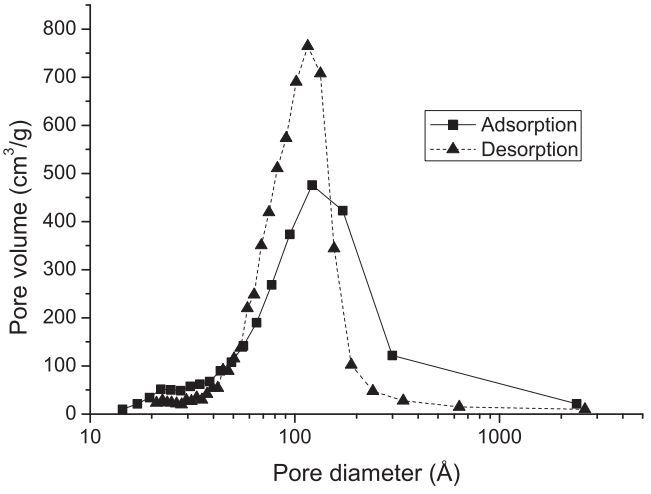

Fig. 4. The nitrogen adsorption–desorption pore volume plots display pore diameters of 10 nm, here for the sample calcined at 400 °C for 2 h.

distribution, usually with the indication of a narrow distribution of pores around 4 nm. In case the experimental isotherm shows signs of pore network effects, the adsorption branch is highly preferred for pore size calculations and is hardly affected by any tensile strength effects. Returning to the adsorption–desorption pore volume plot in Fig. 4 there is no indication of TSE and the pore distribution in both branches show similar results.

3.3. TEM and STEM analysis

The microstructure of the calcined powders was further analyzed by TEM diffraction and high-resolution TEM studies. A representative TEM diffraction pattern and high-resolution TEM micrograph are presented in Fig. 5(a). The spotted ring diffraction pattern and poly-grained structure demonstrate a polycrystalline structure of the powders. To confirm the chemistry of the powders, a X-ray energy dispersive spectrometry (XEDS) was performed. One XEDS result is given in Fig. 5(b), which shows the peaks corresponding to Gd, Ce and O. The quantification analysis averaged from several XEDS spectra revealed that the powders comprised of Ce ($59.61 \pm 1.87\%$) and Gd ($6.01 \pm 1.04\%$). The Ce/Gd-ratio was thus found to be close to the expected value (∼9) in this CGO10 powder. Here, the O content was not considered due to the possible interfering signals from the background epoxy. The Cu signals originated from the supporting Cu grid.

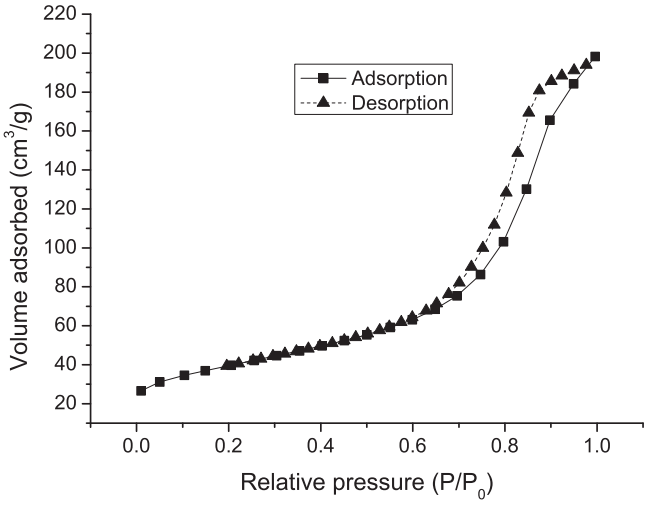

Fig. 3. Nitrogen adsorption–desorption isotherm for CGO10 heat treated at 400 °C.

To obtain a better picture of how the pores were distributed inside the calcined powders the STEM technique was employed. Fig. 6 compares the images of a powder acquired using regular TEM mode (a), STEM BF mode (b), and STEM Z-contrast mode (c) individually. A few locations of pores embedded inside the powders are circled in Fig. 6 for clarification. From Fig. 6, it is evidently shown that the STEM Z-contrast imaging method can provide a better illustration of surface feature and porous morphology with better contrasting between the pores and the particles. The size of the pores was measured to be in the range of 5–20 nm in diameter. These values confirm the pore diameter calculated from the adsorption–desorption pore volume plot in Fig. 4, confirming the presence of mesopores. Considering the similar size range (approximately 10 nm) of both the mesopores and the crystallite size, could suggest that the mesoporosity is formed partly from intergranular porosity and not only due to the presence of the P123 surfactant.

In addition, the valence state of Ce was determined by employing the EELS technique. The background-subtracted and plural scattering removed Ce-$M_{4,5}$ edge EELS spectrum corresponding to the CGO10 powder calcined at 400 °C is shown in Fig. 7. Two features are noticed here. First, the M_4 edge exhibited a higher intensity than the M_5 edge. Second, two satellite peaks (marked with arrows), which individually locate at ∼5 eV behind the main peak, were present. Both findings are typical features for EELS Ce^{4+} $M_{4,5}$ edge and therefore, suggest a +4 state of Ce in this calcined CGO10 powder [23], excluding any uncertainties of non-stoichiometric secondary phases being formed such as e.g. cubic bixbyite, Ce_2O_3.

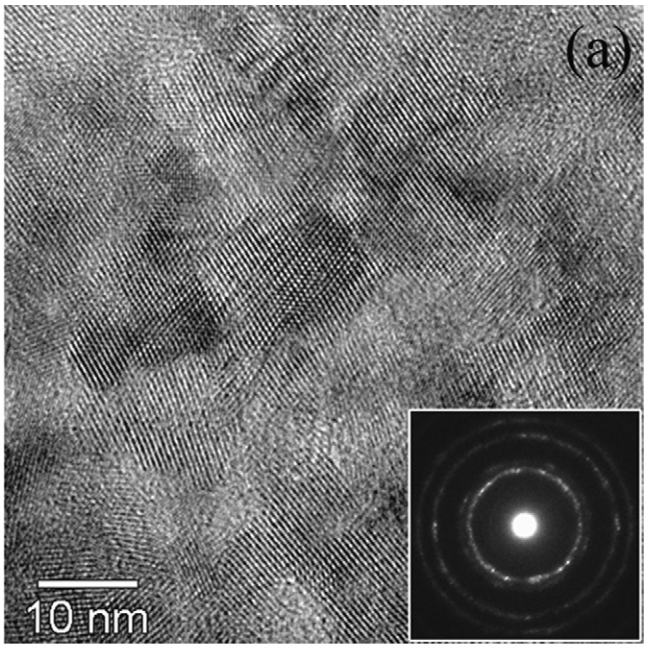

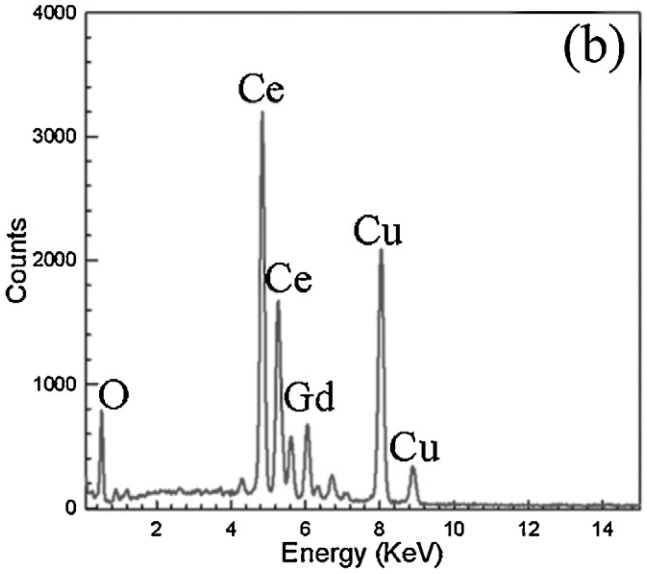

Fig. 5. (a) HREM image and diffraction pattern (inset) and (b) the corresponding XEDS result acquired from CGO powders calcined at 400 °C.

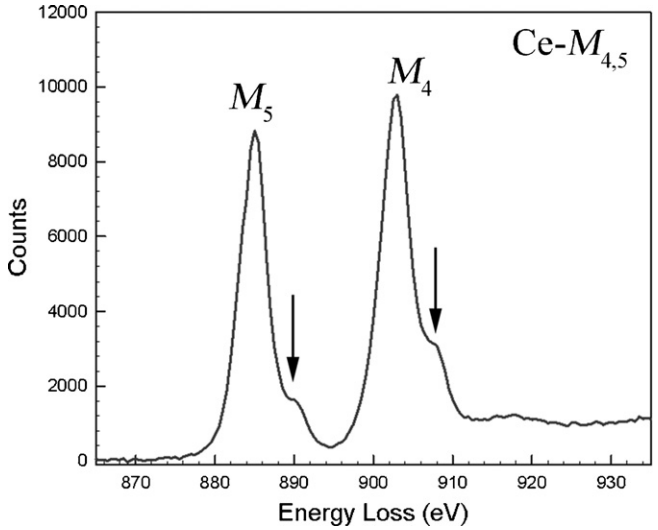

Fig. 7. Ce-$M_{4,5}$ edge corresponding to CGO10 powders calcined at 400 °C.

3.4. Thermal analysis

Fig. 8 shows the results from thermal analysis of the as-spray dried precursor solution. Three major weight loss events were observed. This solution behaves very similar to that without P123 as reported earlier [12], which showed two distinct weight loss events. In both cases, with P123 (as presented in Fig. 8) and without P123 addition [12], the spray dried precursor powders lost weight between 100 °C and 200 °C in an endothermic process as water was evaporated. Further heating of both precursors show a sharp decrease in weight in an endothermic process due to loss of nitrates. Upon further heating to 230 °C and above, the precursor with P123 showed a small weight loss along with a sharp exothermic peak. This small decrease in weight was not observed for similar CGO precursor powder without P123 addition [12]. Therefore, this weight loss is associated with oxidation of P123. This is also consistent with Table 1, where the BET area increases as the calcination temperature is increased from 300 to 400 °C as more pores are opened leading to a higher specific surface area. Furthermore, the exothermic process indicates crystallization of CGO phase. The XRD result in combination with the TEM micrographs and diffraction pattern indicate that crystalline CGO is formed

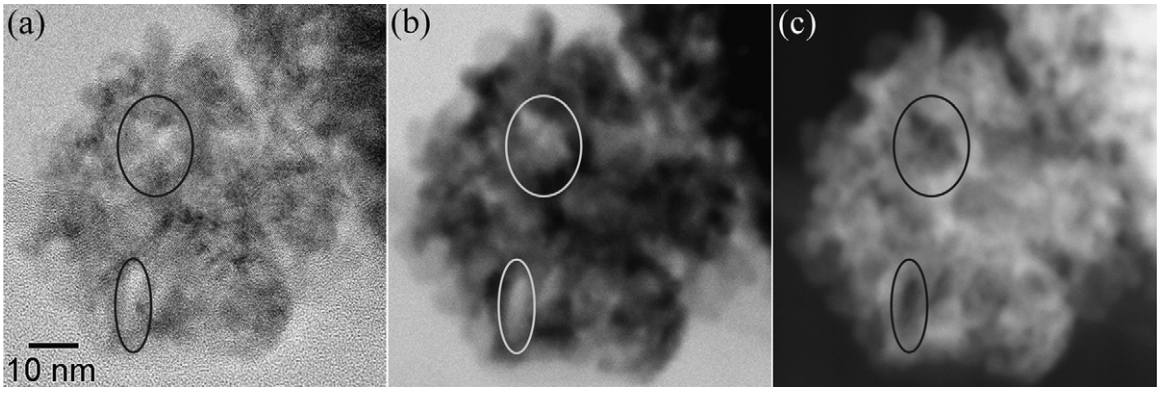

Fig. 6. Comparison of images taken from CGO10 powders calcined at 400 °C with (a) TEM, (b) STEM bright-field, and (c) STEM Z-contrast mode, respectively. The circled areas highlight positions of mesopores.

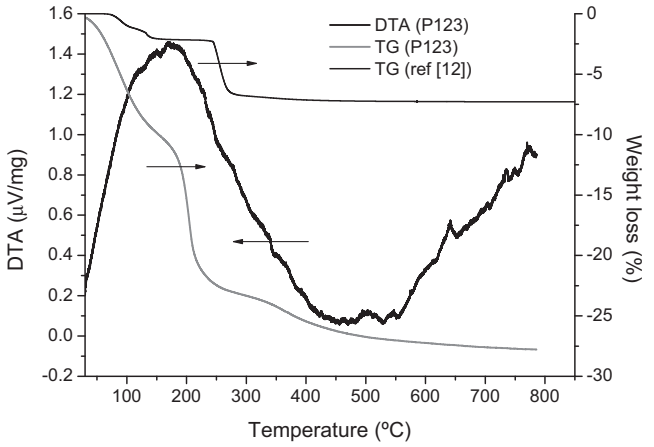

Fig. 8. TG and DTA curves of the as-sprayed CGO10 precursor. The data were taken in flowing air at a heating rate of 5 °C/min. TGA data from Ref. [12] (without P123 in the solution) are inserted for comparison.

already at around 330 °C, which is consistent with the thermal analysis.

Comparison of results presented here to those presented in Ref. [12], show the impact of P123 on the powder characteristics. The BET specific surface area is much higher and the crystallite size smaller when P123 is present in the solution. The crystallization temperature, on the other hand is not affected. Even before the complete removal of P123 at 300 °C, the specific surface area of powders were 104 $m^2\ g^{-1}$ which is significantly higher than that for powders prepared without P123 (68 $m^2\ g^{-1}$) [12]. This clearly shows that the P123 acts as a structure directing agent and can be used for producing high surface area powders.

4. Conclusions

High-surface area crystalline mesoporous CGO powder was synthesized by combining spray drying and a surfactant assisted route followed by calcination. The small droplets formed in the spray drying process are small enough for creation of high surface area mesoporous powders, here CGO, which shows an alternative route for the direct calcination route presented in [1]. Furthermore, as spray drying is a common industrial production method up scaling would be possible.

From TEM and XRD it was evident that the CGO10 powder was crystalline with a crystallite size in the range of 10 nm. This particle size was also confirmed by the high resolution micrographs obtained by SEM. Increasing the calcination temperature from 400 °C to 600 °C showed that the material lost about one third of its surface area, still approximately 100 $m^2\ g^{-1}$ at 600 °C. This makes the material very attractive for low temperature applications in for example catalysis or SOFC components.

References

[1] M. Lundberg, B. Skårman, F. Cesar, L. Reine Wallenberg, Mesoporous thin films of high-surface-area crystalline cerium dioxide, Micropor. Mesopor. Mater. 54 (2002) 97–103.

[2] A. Tschope, W. Liu, M. Flytzanistephanopoulos, J.Y. Ying, Redox activity of nonstoichiometric cerium oxide-based nanocrystalline catalysts, J. Catal. 157 (1995) 42–50.

[3] R.L. Withers, R. Wallenberg, D.J.M. Bevan, J.G. Thompson, B.G. Hyde, The flourite-related solid-solutions of CeO_2–Y_2O_3 II: a modulated structure approach, J. Less Common Met. 156 (1989) 27.

[4] A.E.C. Palmqvist, M. Wirde, U. Gelius, M. Muhammed, Surfaces of doped nanophase cerium oxide catalysts, Nanostruct. Mater. 11 (1999) 995–1007.

[5] E. Mamontov, T. Egami, R. Brezny, M. Koranne, S. Tyagi, Lattice defects and oxygen storage capacity of nanocrystalline ceria and ceria–zirconia, J. Phys. Chem. B 104 (2000) 11110–11116.

[6] B.C.H. Steele, A. Heinzel, Materials for fuel-cell technologies, Nature 414 (2001) 345–352.

[7] B. Dalslet, P. Blennow, P.V. Hendriksen, N. Bonanos, D. Lybye, M. Mogensen, Assessment of doped ceria as electrolyte, J. Solid State Electrochem. 10 (2006) 547–561.

[8] H. Timmermann, D. Fouquet, A. Weber, E. Ivers-Tiffée, U. Hennings, R. Reimert, Internal reforming of methane at Ni/YSZ and Ni/CGO SOFC cermet anodes, Fuel Cells 6 (2006) 307–313.

[9] M. Lundberg, B. Skårman, L. Reine Wallenberg, Crystallography and porosity effects of CO conversion on mesoporous CeO_2, Micropor. Mesopor. Mater. 69 (2004) 187–195.

[10] X. Song, J. Nan, Y. Li, D. Xu, Synthesis and characterization of y-doped mesoporous CeO_2 using a chemical precipitation method, J. Rare Earths 25 (2007) 428–433.

[11] S.J. Lukasiewicz, Spray-drying ceramic powders, J. Am. Ceram. Soc. 72 (1989) 617–624.

[12] P. Blennow, W. Chen, M. Lundberg, M. Menon, Characterization of $Ce_{0.9}Gd_{0.1}O_{1.95}$ powders synthesized by spray drying, Ceram. Int. 35 (2009) 2959–2963.

[13] J.O. Bovin, V. Alfredsson, G. Karlsson, A. Carlsson, Z. Blum, O. Terasaki, TEM-tomography of FAU-zeolite crystals containing Pt-clusters, Ultramicroscopy 62 (1996) 277–281.

[14] I. Langmuir, The adsorption of gases on plane surfaces of glass, mica and platinum, J. Am. Chem. Soc. 40 (1918) 1361–1403.

[15] K.S.W. Sing, D.H. Everett, R.A.W. Haul, L. Moscou, R.A. Pierotti, J. Rouquerol, et al., Reporting physisorption data for gas solid systems with special reference to the determination of surface-area and porosity (recommendations 1984), Pure Appl. Chem. 57 (1985) 603–619.

[16] E.P. Barrett, L.G. Joyner, P.P. Halenda, The determination of pore volume and area distributions in porous substances 1. Computations from nitrogen isotherms, J. Am. Chem. Soc. 73 (1951) 373–380.

[17] P.I. Ravikovitch, S.C.O. Domhnaill, A.V. Neimark, F. Schuth, K.K. Unger, Capillary hysteresis in nanopores: theoretical and experimental studies of nitrogen adsorption on MCM-41, Langmuir 11 (1995) 4765–4772.

[18] C. Lastoskie, K.E. Gubbins, N. Quirke, Pore-size distribution analysis of microporous carbons – a density-functional theory approach, J. Phys. Chem. 97 (1993) 4786–4796.

[19] T. Miyata, A. Endo, T. Ohmori, T. Akiya, M. Nakaiwa, Evaluation of pore size distribution in boundary region of micropore and mesopore using gas adsorption method, J. Colloid Interface Sci. 262 (2003) 116–125.

[20] J. Choma, M. Jaroniec, W. Burakiewicz-Mortka, M. Kloske, Critical appraisal of classical methods for determination of mesopore size distributions of MCM-41 materials, Appl. Surf. Sci. 196 (2002) 216–223.

[21] M. Kruk, M. Jaroniec, A. Sayari, Adsorption study of surface and structural properties of MCM-41 materials of different pore sizes, J. Phys. Chem. B 101 (1997) 583–589.

[22] J.C. Groen, L.A.A. Peffer, J. Perez-Ramirez, Pore size determination in modified micro- and mesoporous materials. Pitfalls and limitations in gas adsorption data analysis, Micropor. Mesopor. Mater. 60 (2003) 1–17.

[23] L.A.J. Garvie, P.R. Buseck, Determination of Ce^{4+}/Ce^{3+} in electron-beam-damaged CeO_2 by electron energy-loss spectroscopy, J. Phys. Chem. Solids 60 (1999) 1943–1947.